

Direct Numerical Simulation of Supersonic Turbulent Boundary Layer over a Compression Ramp

M. Wu* and M. P. Martin†

Princeton University, Princeton, New Jersey 08540

DOI: 10.2514/1.27021

A direct numerical simulation of shock wave and turbulent boundary layer interaction for a 24 deg compression ramp configuration at Mach 2.9 and Re_θ 2300 is performed. A modified weighted, essentially nonoscillatory scheme is used. The direct numerical simulation results are compared with the experiments of Bookey et al. [Bookey, P. B., Wyckham, C., Smits, A. J., and Martin, M. P., "New Experimental Data of STBLI at DNS/LES Accessible Reynolds Numbers," AIAA Paper No. 2005-309, Jan. 2005] at the same flow conditions. The upstream boundary layer, the mean wall-pressure distribution, the size of the separation bubble, and the velocity profile downstream of the interaction are predicted within the experimental uncertainty. The change of the mean and fluctuating properties throughout the interaction region is studied. The low frequency motion of the shock is inferred from the wall-pressure signal and freestream mass-flux measurement.

Nomenclature

a	=	speed of sound
C_f	=	skin friction coefficient
C_k^*	=	optimal weight for stencil k
f	=	frequency
f_s	=	frequency of shock motion
IS_k^*	=	smoothness measurement of stencil k
L_{sep}	=	separation length
M	=	freestream Mach number
p	=	pressure
q_k	=	numerical flux of candidate stencil k
Re_δ	=	Reynolds number based on δ
Re_θ	=	Reynolds number based on θ
r	=	number of candidate stencils in WENO
S_L	=	dimensionless frequency of shock motion
T	=	temperature
u	=	velocity in the streamwise direction
v	=	velocity in the spanwise direction
w	=	velocity in the wall-normal direction
x	=	coordinate in the streamwise direction
y	=	coordinate in the spanwise direction
z	=	coordinate in the wall-normal direction
δ	=	99% thickness of the incoming boundary layer
δ^*	=	displacement thickness of the incoming boundary layer
θ	=	momentum thickness of the incoming boundary layer
ρ	=	density
ω_k	=	weight of candidate stencil k

Subscripts

w	=	value at the wall
∞	=	freestream value

Superscript

* = nondimensional value

I. Introduction

MANY aspects of shock wave and turbulent boundary layer interaction (STBLI) are not fully understood, including the dynamics of shock unsteadiness, turbulence amplification and mean flow modification induced by shock distortion, separation and reattachment criteria as well as the unsteady heat transfer near the separation and reattachment points, and the generation of turbulent mixing layers and underexpanded jets in the interaction region, especially when they impinge on a surface. Yet, STBLI problems are of great importance for the efficient design of scramjet engines and control surfaces in hypersonic vehicles. A more profound understanding of STBLI will lead to flow control methodologies and novel hypersonic vehicle designs.

Different canonical configurations have been used in STBLI studies. The compression ramp configuration has been studied extensively experimentally, and there are numerous experimental data available for this configuration. For example, Settles et al. [1–3] studied 2-D/3-D compression ramp and sharp fin STBLI problems in detail. Dolling et al. [4,5] studied the unsteadiness for compression ramp configurations, and Selig [6] studied the unsteadiness of STBLI and its control for a 24 deg compression ramp. Recently, Bookey et al. [7] performed experiments on a 24 deg compression ramp configuration with flow conditions accessible for direct numerical simulation (DNS) and large eddy simulation (LES), which provides valuable data for the validation of our simulations.

In contrast with numerous experimental data, there are few detailed numerical simulations such as DNS and LES. Numerical simulations of STBLI have been mainly confined to Reynolds averaged Navier–Stokes simulation (RANS) due to the limitation of computational resources. However, RANS is shown not capable of predicting the wall pressure or the heat flux within a satisfactory accuracy for shock interactions. Settles et al. [2] compared experimental results with those of a one-equation model RANS for the compression ramp configuration and showed that there were significant differences in the wall-pressure distribution when the flow was separated. Zheltovodov [8] showed that the state-of-the-art RANS models do not give accurate predictions for strong STBLI. The unsteady nature of STBLI problems is believed to account for the discrepancies between RANS and experiments. DNS and LES of STBLI have existed for less than a decade. Knight et al. [9] compiled a summary of existing LES for the compression ramp configuration and concluded that LES did not predict the wall pressure or the separation length accurately in separated flows. In 2000, Adams [10] performed the first DNS for an 18 deg compression ramp flow at

Received 3 August 2006; revision received 27 December 2006; accepted for publication 27 December 2006. Copyright © 2007 by the authors. Published by the American Institute of Aeronautics and Astronautics, Inc., with permission. Copies of this paper may be made for personal or internal use, on condition that the copier pay the \$10.00 per-copy fee to the Copyright Clearance Center, Inc., 222 Rosewood Drive, Danvers, MA 01923; include the code 0001-1452/07 \$10.00 in correspondence with the CCC.

*Graduate Student, Mechanical and Aerospace Engineering Department, Student Member AIAA.

†Assistant Professor, Mechanical and Aerospace Engineering Department, Member AIAA.

$M = 3$ and $Re_\theta = 1685$. Because of the lack of experimental data at the same flow conditions, Adams was not able to draw definite conclusions by comparing his DNS with higher Reynolds number experiments. The same is true for the LES of STBLI induced by a compression corner of Rizzetta and Visbal [11]. In 2004, Wu and Martin [12] performed DNS for a 24 deg compression ramp configuration. The DNS results were compared with experiments from Bookey et al. [7] at the same flow conditions. Significant discrepancies were found in the size of the separation bubble and the mean wall-pressure distribution [13]. Given the stringent constraints in grid size for affordable DNS of STBLI, the numerical dissipation of the original WENO (weighted essentially nonoscillatory) method [14,15] was found responsible for these discrepancies [16].

Experiments of STBLI have shown evidence of large scale, slow shock motion. The characteristic time scale for the motion is of the order of $10\delta/U_\infty$, which is 1 order of magnitude greater than the characteristic time scale of the incoming boundary layer. Dussauge et al. [17] compiled frequencies that were found in experiments for different configurations and found that the dimensionless frequency of the shock motion is mainly between 0.02 and 0.05. The dimensionless frequency is defined as

$$S_L = f_s L_{sep}/U_\infty \quad (1)$$

A complete physical explanation of the low frequency motion remains an open question. Andreopoulos and Muck [18] studied the shock unsteadiness of a compression ramp configuration. They concluded that the shock motion is driven by the bursting events in the incoming boundary. Recently, Ganapathisubramani et al. [19] proposed that very long coherent structures of high and low momentum are present in the incoming boundary layer and are responsible for the low frequency motion of the shock. These structures can be as long as 40δ and meander in the spanwise direction. Despite the existence of large scale slow motion of the shock that is found in experiments, no evidence has been reported in previous numerical simulations.

In this paper, we present new DNS data for a 24 deg compression ramp STBLI configuration. The governing equations and flow conditions are presented in Secs. II and III, respectively. The modifications to the original WENO method are described in Sec. IV, and the accuracy of the DNS data by comparison against experimental data [7] at the same conditions is reported in Sec. V. The shock motion, including evidence of low frequency motion, is described in Sec. VI.

II. Governing Equations

The governing equations are the nondimensionalized conservative form of the continuity, momentum, and energy equations in curvilinear coordinates. The working fluid is air, which is assumed to be a perfect gas.

$$\frac{\partial \mathbf{U}}{\partial t} + \frac{\partial \mathbf{F}}{\partial \xi} + \frac{\partial \mathbf{G}}{\partial \eta} + \frac{\partial \mathbf{H}}{\partial \zeta} = 0 \quad (2)$$

where

$$\mathbf{U} = J \begin{Bmatrix} \rho^* \\ \rho^* u^* \\ \rho^* v^* \\ \rho^* w^* \\ \rho^* e^* \end{Bmatrix}, \quad \mathbf{F} = \mathbf{F}_c + \mathbf{F}_v \quad (3)$$

and

$$\mathbf{F}_c = Jr_\xi \begin{Bmatrix} \rho^* u^* \\ \rho^* u^* u^* + p^* s_x^* \\ \rho^* v^* u^* + p^* s_y^* \\ \rho^* w^* u^* + p^* s_z^* \\ (\rho^* e^* + p^*) u^* \end{Bmatrix}$$

$$\mathbf{F}_v = -Jr_\xi \begin{Bmatrix} 0 \\ \sigma_{xx}^* s_x + \sigma_{xy}^* s_y + \sigma_{xz}^* s_z \\ \sigma_{yx}^* s_x + \sigma_{yy}^* s_y + \sigma_{yz}^* s_z \\ \sigma_{zx}^* s_x + \sigma_{zy}^* s_y + \sigma_{zz}^* s_z \\ (\sigma_{xx}^* u + \sigma_{xy}^* v + \sigma_{xz}^* w) s_x^* + \\ (\sigma_{yx}^* u + \sigma_{yy}^* v + \sigma_{yz}^* w) s_y^* + \\ (\sigma_{zx}^* u + \sigma_{zy}^* v + \sigma_{zz}^* w) s_z^* - \\ q_x^* s_x^* - q_y^* s_y^* - q_z^* s_z^* \end{Bmatrix} \quad (4)$$

and

$$s_x^* = \xi_x/r_\xi^*, \quad u^* = u^* s_x^* + v^* s_y^* + w^* s_z^*$$

$$r_\xi^* = \sqrt{\xi_x^2 + \xi_y^2 + \xi_z^2} \quad (5)$$

In curvilinear coordinates, flux terms G and H have similar forms as F . σ_{ij}^* is given by the Newtonian linear stress-strain relation:

$$\sigma_{ij}^* = \frac{1}{Re_\delta} \left(2\mu^* S_{ij}^* - \frac{2}{3}\mu^* \delta_{ij} S_{kk}^* \right) \quad (6)$$

The heat flux terms q_j^* are given by Fourier law:

$$q_j^* = -\frac{1}{Re_\delta} k^* \frac{\partial T^*}{\partial x_j^*} \quad (7)$$

The dynamic viscosity is computed by Sutherland's law:

$$\mu = 1.458 \times 10^{-6} T^{3/2}/(T + 110.3) \quad (8)$$

The nondimensionalization is done by $\rho^* = \rho/\rho_\infty$, $u^* = u/U_\infty$, $e^* = e/U_\infty^2$, $p^* = p/\rho_\infty U_\infty^2$, and $T^* = T/T_\infty$, and $\mu^* = \mu/\mu_\infty$. Incoming boundary layer thickness δ is used as the characteristic length scale.

III. Flow Configuration

Figure 1 shows an inviscid flow schematic for the present STBLI configuration. The incoming flow conditions are listed in Table 1, including the reference experiment of Bookey et al. [7] for the same flow.

To minimize numerical errors in the computation of Jacobian matrices, we generate the grid using analytical transformations. Details about the transformation can be found in Wu and Martin [12]. A sample grid is plotted in Fig. 2. The grid is clustered near the corner in the streamwise direction and near the wall in the wall-normal direction. The size of the computational domain is shown in Fig. 3. There are 9δ and 7δ upstream and downstream of the corner in the streamwise direction, 2.2δ in the spanwise direction, and 5δ in the wall-normal direction. The number of grid points used is $1024 \times 160 \times 128$ in the streamwise, spanwise, and wall-normal directions, respectively. The largest and smallest grid spacings in the streamwise direction are $\Delta x^+ = 7.2$ and $\Delta x^+ = 3.4$, respectively, with grid points clustered near the corner. The grid spacing in the spanwise direction is $\Delta y^+ = 4.1$. In the wall-normal direction at the inlet, the first grid is at $z^+ = 0.2$ and there are 28 grid points within $z^+ < 20$.

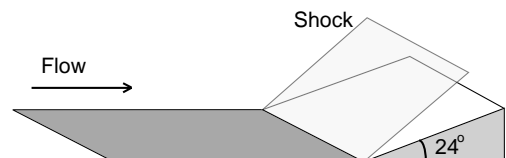


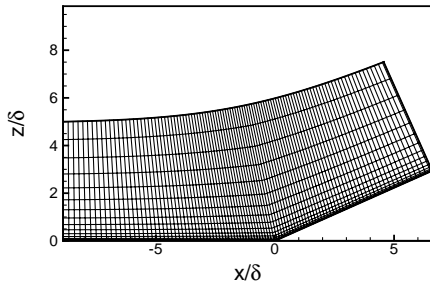
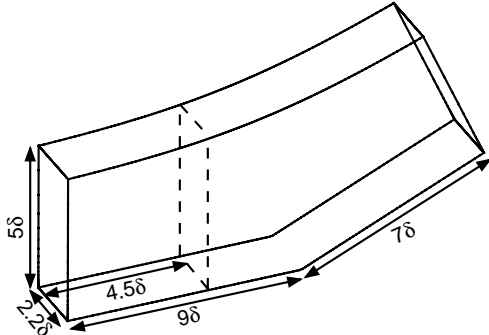
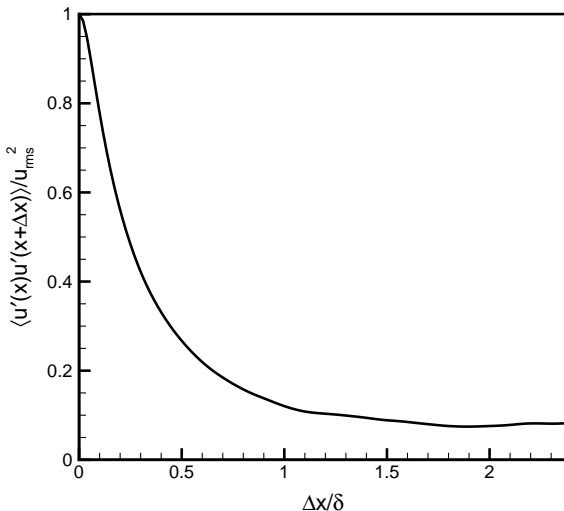
Fig. 1 Inviscid flow schematic for the compression ramp case.

Table 1 Conditions for the incoming turbulent boundary layer

	M	Re_θ	θ , mm	δ^* , mm	C_f	δ , mm	ρ_∞ , kg/m ³	U_∞ , m/s	T_∞ , K
Experiment [7]	2.9	2400	0.43	2.36	0.00225	6.7	0.074	604.5	108.1
DNS	2.9	2300	0.38	1.80	0.00217	6.4	0.077	609.1	107.1

IV. Numerical Method and Boundary Conditions

A third-order accurate low-storage Runge–Kutta method is used for the time integration, and a fourth-order accurate central standard finite difference scheme is used to compute the viscous flux terms. The incoming boundary layer is generated as in Martin [20]. The rescaling method developed by Xu and Martin [21] is used to generate the inflow condition. The recycling station is located at 4.5δ downstream of the inlet. Figure 4 plots the autocorrelation of u' in the streamwise direction. The correlation decreases to 0.1 in about 1.2δ . In turn, we find that the recycling station can be located as close as 2δ

**Fig. 2** Sample grid for the DNS.**Fig. 3** Size of the computational domain for the DNS.**Fig. 4** Autocorrelation of u' in the streamwise direction at $z = 0.18$ in the incoming boundary layer for the DNS.

downstream of the inlet without affecting the statistics of the boundary layer. The data indicate that there is no forcing frequency imposed by the rescaling method, as discussed further in Sec. VI. Supersonic outflow boundary conditions are used at the outlet and the top boundary. We use a nonslip condition at the wall, which is isothermal. The wall temperature is set to 307 K. Details about initial and boundary conditions can be found in [12,13]. To compute the convective flux terms, we modify a fourth-order bandwidth-optimized WENO [15] method by adding limiters [22]. Later, we present a brief description of the original WENO method and how the limiters are used.

In WENO methods, the numerical fluxes are approximated by the weighted sum of fluxes on the candidate stencils. Figure 5 plots a sketch of the WENO three-point candidate stencils. The numerical flux can be expressed as

$$f_{i+\frac{1}{2}} = \sum_{k=0}^r \omega_k q_k^r \quad (9)$$

where q_k^r are the candidate fluxes at $(i + 1/2)$ and ω_k are the weights. The weights are determined by the smoothness on each candidate stencil, where the smoothness is measured by

$$IS_k = \sum_{m=1}^{r-1} \int_{x_{i-1/2}}^{x_{i+1/2}} (\Delta x)^{2m-1} \left(\frac{\partial^m q_k^r}{\partial x^m} \right)^2 dx \quad (10)$$

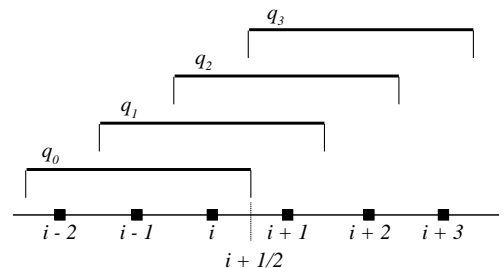
Thus, larger weights are assigned to stencils with smaller IS_k . For the three-point per candidate stencil WENO shown in Fig. 5, Taylor expansion of the above equation gives

$$IS_k = (f'_i \Delta x)^2 [1 + \mathcal{O}(\Delta x^2)] \quad (11)$$

This means that in smooth regions for a well-resolved flowfield [meaning f'_i is $\mathcal{O}(1)$], IS_k is of the order of Δx^2 , while for a discontinuity, IS_k is of the order of 1. Details about the formulation of WENO methods can be found in Jiang and Shu [23] and Martin et al. [15], for example.

Previous work on WENO methods has been focused on maximizing the bandwidth resolution and minimizing the dissipation of the candidate stencils, that is, optimizing the linear part of WENO methods. Examples include Weirs [14] and Martin [15]. The numerical dissipation inherent in such methods can be avoided by increasing the mesh size, which results in accurate results for isotropic turbulence and turbulent boundary layers [15]. In stringent problems such as STBLI, increasing the grid size is not affordable and the numerical dissipation inherent in original WENO methods precludes obtaining accurate results [16].

To mitigate the problem, we add limiters in the smoothness measurement [22], namely, absolute limiter and relative limiter. The definitions are shown in Eqs. (12) and (13), respectively,

**Fig. 5** Sketch of WENO candidate stencils with three points per candidate.

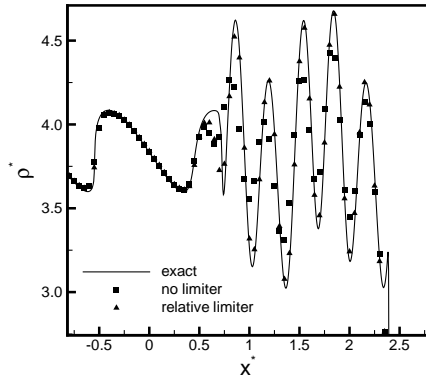


Fig. 6 Density distribution at $t = 1.8$ for the Shu–Osher’s problem with and without the relative smoothness limiter.

$$\omega_k = \begin{cases} C_k^r, & \text{if } \max(IS_k) < A_{AL} \\ \omega_k, & \text{otherwise} \end{cases} \quad (12)$$

$$\omega_k = \begin{cases} C_k^r, & \text{if } \max(IS_k) / \min(IS_k) < A_{RL} \\ \omega_k, & \text{otherwise} \end{cases} \quad (13)$$

where C_k^r are the optimal weights [15] and A_{AL} and A_{RL} are the thresholds for the limiters. It is found that the relative limiter is more general and less problem dependent [22]. In contrast, the relative limiter defined by Eq. (13) is method dependent, that is, WENO methods with different candidate stencil sizes have different threshold values in the relative limiter. Thus, we define an alternative relative limiter:

$$\omega_k = \begin{cases} C_k^r, & \text{if } \max(TV_k) / \min(TV_k) < A_{RL}^{TV} \\ \omega_k, & \text{otherwise} \end{cases} \quad (14)$$

where TV_k stands for the total variation on each candidate stencil. This new definition allows for consistent threshold values of about 5 in the relative limiter, independently of the stencil size. The improved performance of the limiter (14) for the fourth-order bandwidth-optimized WENO scheme is illustrated by computing the Shu–Osher problem [24]. The initial conditions are

$$\begin{cases} \rho_i^* = 3.86, & \rho_r^* = 1 + 0.2 \sin(5x) \\ u_i^* = 2.63, & u_r^* = 0 \\ p_i^* = 10.33, & p_r^* = 1 \end{cases} \quad (15)$$

Figure 6 plots the results at $t = 1.8$. The line is the converged numerical result using 1600 grid points. The square and triangle symbols are the computed results with and without the relative limiter, respectively, using 200 grid points. It is clear that the result with the relative limiter is much better in the high frequency fluctuation region, where the resolution is poor.

We also find that the absolute limiter alone improves our DNS results for the compression ramp case [16]. In what follows, we show that using both the limiters at the same time reduces the numerical dissipation further, thereby improving the DNS results. According to the definition of both the limiters, we see they have different effects on reducing the numerical dissipation. To show the effects of applying the limiters more clearly, 2-D nonlinearity index contour plots computed in the wall-normal direction for the DNS of the compression ramp case are shown in Fig. 7. The nonlinearity index is defined as [25]

$$NI = \frac{1}{(r(r+1))^{1/2}} \left[\sum_{k=0}^r \left(\frac{[1/(r+1)] - [(\omega_k/C_k^r) / \sum_{k=0}^r (\omega_k/C_k^r)]}{[1/(r+1)]} \right)^2 \right]^{1/2} \quad (16)$$

where r is the number of candidate stencils. The nonlinearity index has a value in the range of $[0, 1]$. The magnitude of NI indicates how much dissipation is added by WENO. The smaller NI is, the less dissipation is added. Ideally, NI should be zero everywhere except for regions near discontinuities. Figure 7a shows that without any limiter, the nonlinearity index has high values in a very large region of the computational domain. Because in WENO methods, numerical fluxes are computed in characteristic space, the NI values plotted here are also computed in characteristic space for the characteristic equation with eigenvalue equal to $u + a$. The average NI value is about 0.5. With the absolute limiter added, the dissipation is reduced greatly, as shown in Fig. 7b. The average NI value is 0.09. The same plot with the relative limiter is shown in Fig. 7c. The average NI value is also about 0.09 for this case. With both the relative and absolute limiters, as shown in Fig. 7d, the average NI value is 0.02, indicating that the numerical dissipation is further

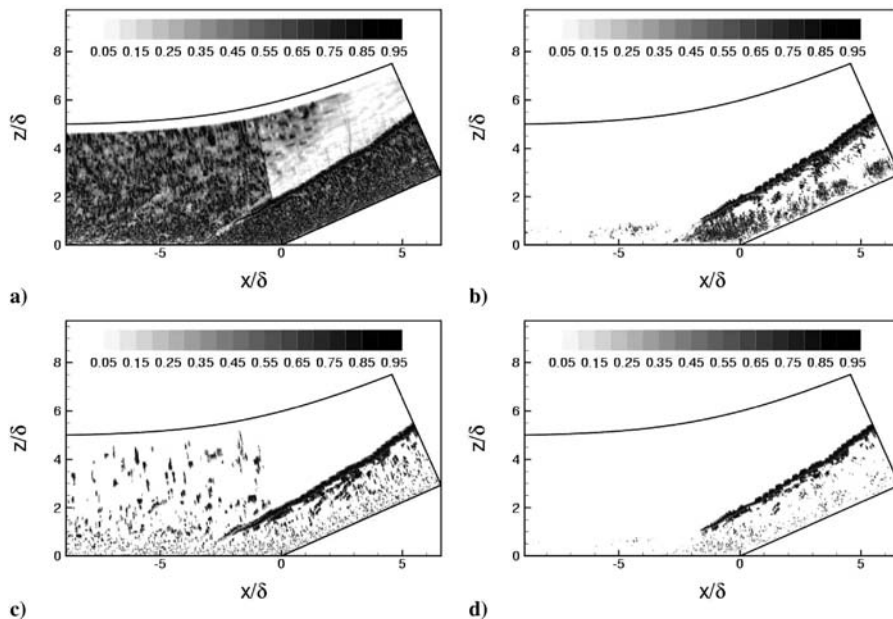


Fig. 7 Nonlinearity index for the compression ramp case: a) without limiters, b) with the absolute limiter, c) with the relative limiter, and d) with both the relative and absolute limiters from DNS.

reduced. In the DNS, we apply both limiters. However, the simulation can be unstable, and we find that this can be avoided by changing the relative limiter to

$$\omega_k = \begin{cases} C_k^r, & \text{if } \max(\text{TV}_k)/\min(\text{TV}_k) < A_{\text{RL}}^{\text{TV}} \text{ and } \max(\text{TV}_k) < B_{\text{RL}}^{\text{TV}} \\ \omega_k, & \text{otherwise} \end{cases} \quad (17)$$

The additional threshold value $B_{\text{RL}}^{\text{TV}}$ guarantees enough dissipation whenever $\max(\text{TV}_k)$ is larger than the threshold. The threshold values are $A_{\text{AL}} = 0.01$, $A_{\text{RL}}^{\text{TV}} = 5$, and $B_{\text{RL}}^{\text{TV}} = 0.2$ in the DNS. A study of WENO methods including limiters for DNS of compressible turbulence is given in Taylor et al. [22].

V. Accuracy of the DNS

DNS statistics are gathered using 300 flowfields with time intervals equal to $1\delta/U_\infty$. Figure 8 plots the spanwise energy spectrum of u at $z^+ = 15$ for the incoming boundary layer. The Reynolds number for the DNS is relatively low. Therefore no obvious inertial range is observed in the spectrum. Over five decades of decay are observed in the energy and no pileup of energy due to numerical error is observed in the high frequency range. The DNS results are compared with the experiments of Bookey et al. [7]. Figure 9 plots the mean wall-pressure distribution. Repeatability studies [6] indicate an experimental uncertainty of about 5%. The DNS data predict the wall-pressure distribution within the experimental uncertainty. Figure 10 plots the nondimensionalized

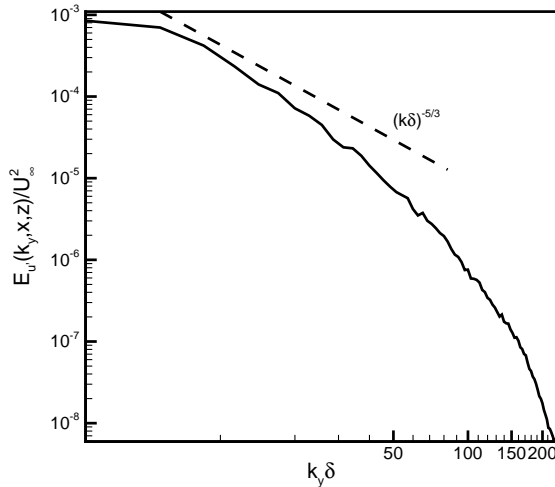


Fig. 8 Spanwise energy spectrum of u at $z^+ = 15$ in the incoming boundary layer for the DNS.

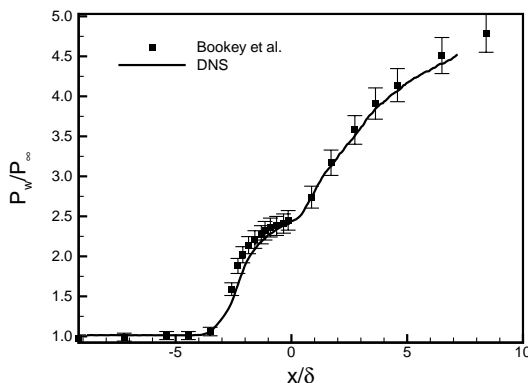


Fig. 9 Mean wall-pressure distribution from DNS and experimental data, error bars at 5%.

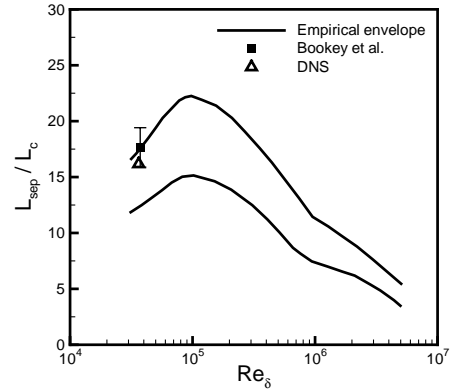


Fig. 10 Size of the separation bubble from DNS and experimental data, error bars at 10%.

size of the separation bubble versus Reynolds number. In the DNS, the separation and reattachment points are defined as the points where the mean skin friction coefficient changes sign. The experimental value is inferred from surface oil visualization. The error on the experimental value is hard to quantify from this technique and it can easily be 10%,[‡] which corresponds to the error bar in Fig. 10. The empirical envelope is from Zheltovodov et al. [26] who correlated the size of the separation bubble for a large set of experimental data. The characteristic length is defined as [26]

$$L_c = \frac{\delta}{M^3} \left(\frac{p_2}{p_{\text{pl}}} \right)^{3.1} \quad (18)$$

where p_2 is the downstream inviscid pressure, and p_{pl} is the plateau pressure computed according to the empirical formula by Zukoski [27]

$$p_{\text{pl}} = p_\infty \left(\frac{1}{2} M + 1 \right) \quad (19)$$

The data points for the DNS and the reference experiment both lie within the empirical envelope. The difference between them is about 10%. The predicted separation and reattachment points are at $x = -3\delta$ and $x = 1.3\delta$, respectively (the corner is located at $x = 0$). In the experiment of Bookey et al., the separation and reattachment points are at $x = -3.2\delta$ and $x = 1.6\delta$, respectively.

Figure 11a plots velocity profiles from the DNS and the experiments of Bookey et al. [7] in the incoming boundary layer. Figure 11b plots velocity profiles 4δ downstream of the corner, where the velocity is nondimensionalized by that at the boundary layer edge. There is a 5% uncertainty in the experimental measurement for the boundary layer thickness,[§] as shown in the error bar. For both the upstream and downstream data, the agreement is within 5%. Figure 12 plots mass-flux turbulence intensities at different streamwise locations for the DNS. Downstream of the interaction, we see that the maximum of the mass-flux turbulence intensity is amplified by a factor of 5, which is consistent with the number 4.8 that Selig et al. [28] found in experiments. Notice that the experiments of Selig et al. are at a much higher Reynolds number ($Re_\theta = 85,000$). However, the Mach number and ramp angle are the same. Therefore the pressure rise throughout the interaction region is the same. Assuming that the mass-flux turbulence intensity amplification is mainly a function of pressure rise, it is reasonable to make the above comparison.

Figure 13 plots Van Driest transformed mean velocity profiles at different streamwise locations. Near the inlet of the computational domain ($x = -8\delta$), the profile agrees well with the log law in the logarithmic region. The profile does not change at $x = -4.1\delta$, which is about 1δ upstream of the separation location. Downstream of the interaction, the profiles show characteristic dips in the logarithmic

[‡]Smits, A., private communication, 2006.

[§]Smits, A., private communication, 2006.

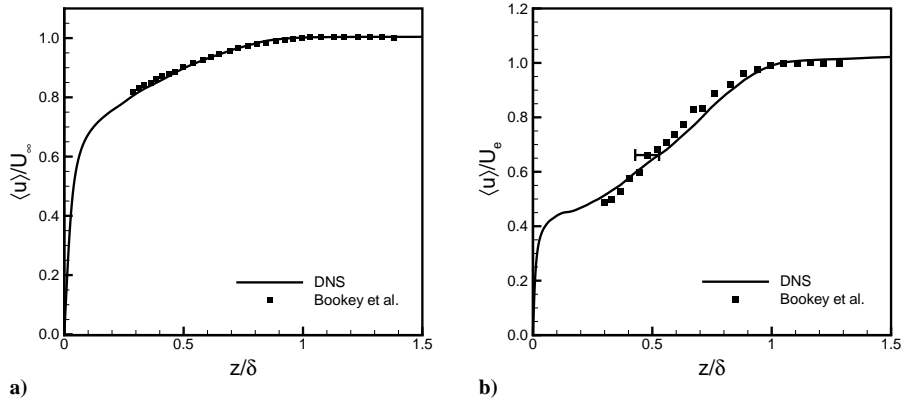


Fig. 11 Velocity profiles in the incoming boundary layer a) and 4δ downstream of the corner b) from DNS and experimental data. The error bar indicates a 5% error in the measurement for the boundary layer thickness.

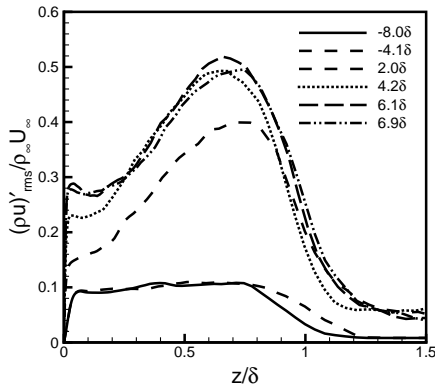


Fig. 12 Mass-flux turbulence intensities at different streamwise locations for the DNS.

region, which is consistent with what Smits and Muck [29] found in higher Reynolds number ($Re_\theta = 85,000$) experiments.

VI. DNS Results

Figure 14 is an instantaneous isosurface contour plot of the magnitude of pressure gradient $|\nabla p| = 0.5$ for the DNS. It shows the 3-D shock structure. Except for the foot of the shock, which is inside the boundary layer edge, the shock is quite flat in the spanwise direction. Also a few shocklets that merge into the main shock are visible downstream of the corner. They are formed due to the compression at the reattachment point.

Figure 15 plots an instantaneous numerical schlieren plot, in which the variable is defined as

$$NS = c_1 \exp[-c_2(x - x_{min}) / (x_{max} - x_{min})] \quad (20)$$

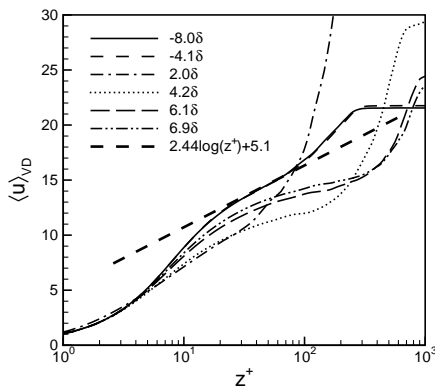


Fig. 13 Van Driest transformed mean velocity profiles at different streamwise locations for the DNS.

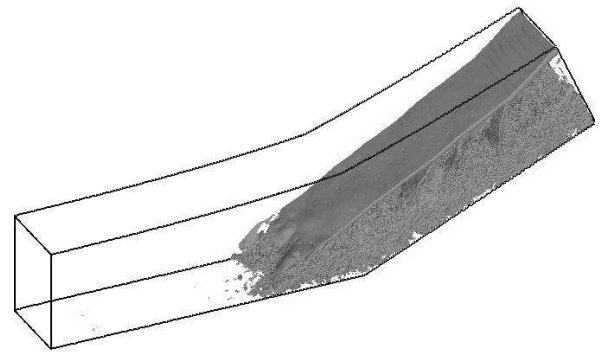


Fig. 14 Contour plot of the magnitude of pressure gradient, $|\nabla p| = 0.5 P_\infty / \delta$, showing the 3-D shock structure for the DNS.

where $x = |\nabla \rho|$, and c_1 and c_2 are constants. We use $c_1 = 0.8$ and $c_2 = 10$ in our analysis. This transformation enhances small density gradients in the flow field and resembles schlieren in experiments. As shown in Fig. 15, the main shock wrinkles and the shock foot penetrates into the boundary layer. A few shocklets emanate from the edge of the boundary layer downstream of the interaction and they merge into the main shock eventually. The turbulence structures in the incoming boundary layer and downstream of the interaction are

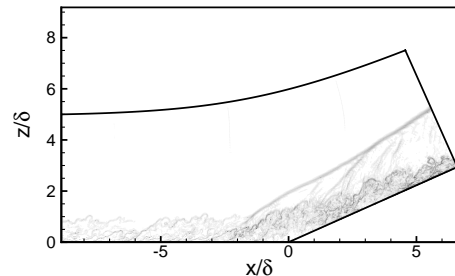


Fig. 15 Instantaneous numerical schlieren plot for the DNS.

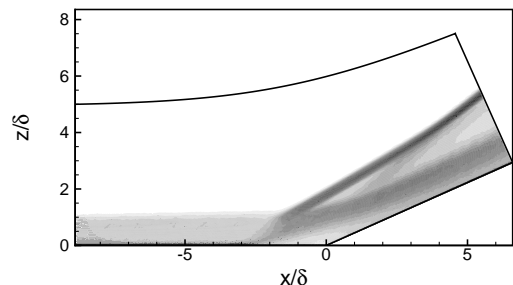


Fig. 16 Time and spanwise averaged numerical schlieren plot for the DNS.

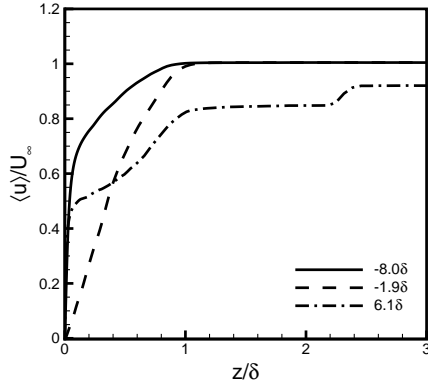


Fig. 17 Velocity profiles at three different streamwise locations for the DNS.

clearly seen. Downstream of the interaction, the gradients are steeper, showing the turbulence amplification due to the flow through the shock. Figure 16 plots the time and spanwise averaged numerical schlieren. The turning of the flow at the separation bubble upstream of the corner, results in the first portion of the main shock, which is at 29 deg and corresponds to an 11 deg turning angle. Near the reattachment point, the flow is turned again by the ramp wall. The compression waves can also be seen in Fig. 16. These waves are the averaged shocklets shown in Fig. 15. They merge into the main shock at a location of about 4δ downstream of the corner and change the angle of the main shock. The second part of the shock has an angle of about 37 deg, which is still less than that of an inviscid shock angle (43 deg). This is because the computational domain is not long enough to let the shock evolve further. Notice that the shock appears thicker in Fig. 16, indicating the motion of the main shock.

A. Evolution of the Boundary Layer

As shown in Fig. 13, streamwise velocity profiles change greatly throughout the interaction region. Figure 17 plots three velocity profiles at different streamwise locations using outer scales. For the profile at $x = -1.9\delta$, which is inside the separation region, the velocity profile is very different from that at the inlet. It has a linear behavior. Downstream of the interaction, at $x = 6.1\delta$, the boundary layer profile is not recovered. Also notice that there is no visible oscillation near the shock, which means that the limiters presented in Sec. III do not affect the good shock-capturing properties of WENO.

Turbulent fluctuations are amplified through the interaction region. Figure 18 plots four components of the Reynolds stresses at different streamwise locations. Downstream of the interaction, all the

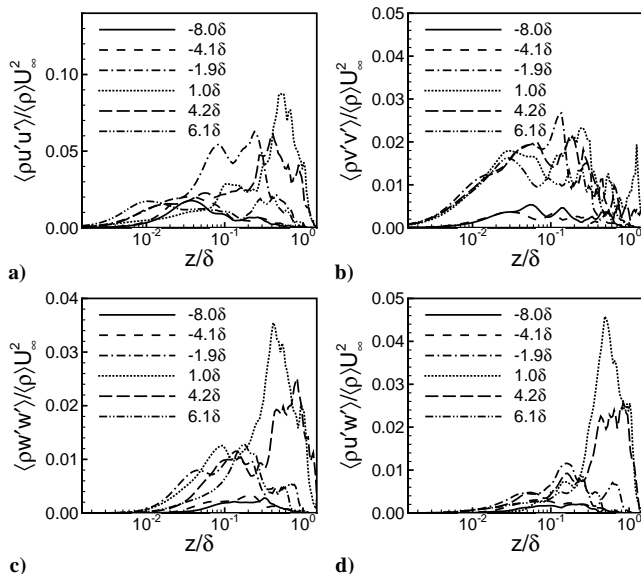


Fig. 18 Reynolds stresses at different streamwise locations for the DNS.

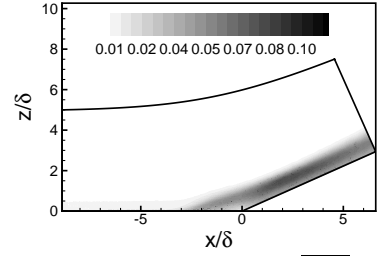


Fig. 19 Contours of the time-averaged TKE $\overline{\rho u' u'}/2\rho_\infty U_\infty^2$ level for the DNS.

components are amplified greatly. In particular, components $\rho u' u'$ and $\rho v' v'$ are amplified by factors of about 6, as shown in Figs. 18a and 18b. Component $\rho w' w'$ is amplified by a factor of about 12. Component $\rho u' w'$ has the largest amplification factor of about 24. As being discussed in the previous section, mass-flux turbulence intensity is amplified by a factor of about 5. Figure 19 plots the time-averaged TKE (turbulent kinetic energy) in the streamwise-wall-normal plane. In the incoming boundary layer, the TKE level is low and the maximal value occurs very close to the wall. The TKE is amplified through the interaction region. Inside the separation bubble near the ramp corner, the TKE level is low. Downstream of the interaction, the TKE is greatly amplified.

Morkovin's SRA (strong Reynolds analogy) is well known for compressible turbulent boundary layer flows. The SRA relations are given by

$$\frac{\sqrt{\tilde{T}^{\prime 2}}}{\tilde{T}} = (\gamma - 1)M^2 \frac{\sqrt{u^{\prime 2}}}{\tilde{u}} \quad (21)$$

$$R_{uT} = \frac{-\overline{u'T'}}{\sqrt{u^{\prime 2}}\sqrt{T^{\prime 2}}} = \text{const} \quad (22)$$

where a tilde in the equations denotes Favre average. Figure 20 shows $T'_{\text{rms}}\tilde{u}/(\gamma - 1)M^2 u'_{\text{rms}}\tilde{T}$ and R_{uT} at different streamwise locations. Upstream of the separation region, Fig. 20a, the SRA relations are satisfied except in the very near wall region and the region close to the boundary layer edge. Figures 20b and 20c show the data inside the interaction region. We observe that the SRA relations are still valid in the outer part of the boundary layer ($z > 0.5\delta$). While in the near wall region, the SRA cannot be applied. The location of the last plot in Fig. 20d is 6.1δ away from the ramp corner, which is very close to the outlet. The two quantities show a

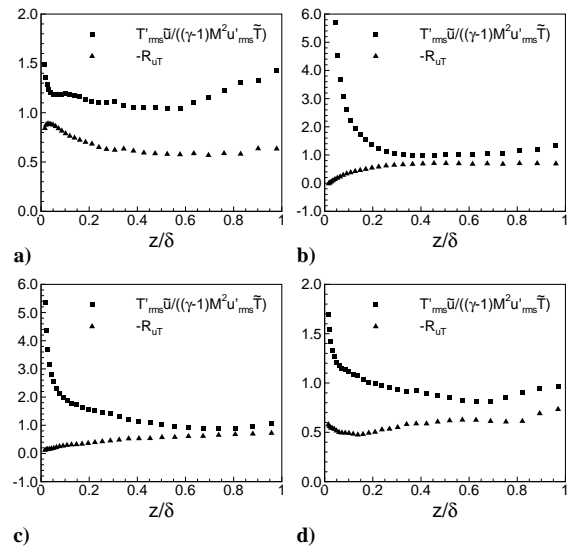


Fig. 20 SRA Eqs. (21) and (22) at different streamwise locations for the DNS: a) $x = -5.7\delta$; b) $x = -2\delta$; c) $x = 2\delta$; d) $x = 6.1\delta$.

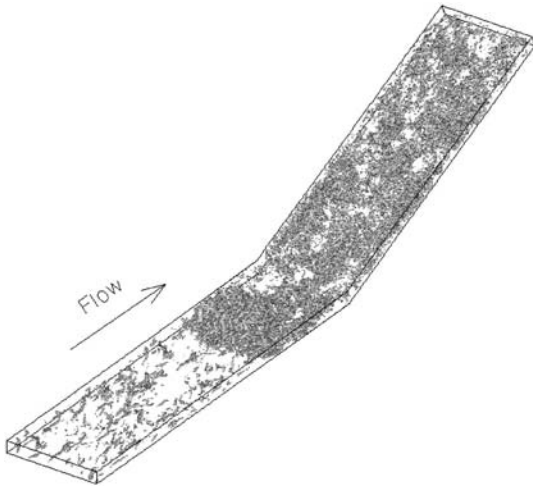


Fig. 21 Isosurface of the discriminant of the velocity gradient tensor for the DNS. Isosurface value is 10^{-5} that of the maximum value.

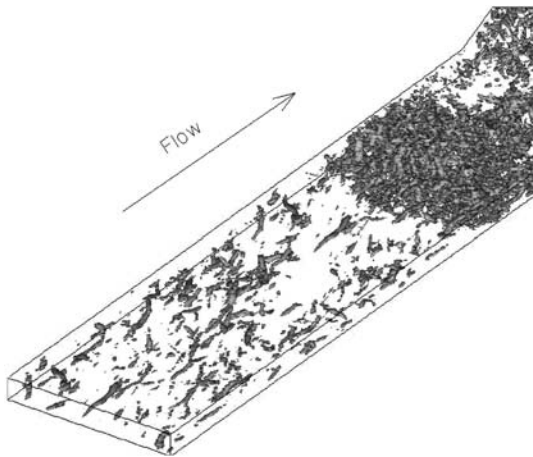


Fig. 22 Isosurface of the discriminant of the velocity gradient tensor upstream of the ramp corner for the DNS. Zoomed visualization of Fig. 21.

trend of going back to their values upstream of the interaction; however, these still deviate from the SRA relations. This indicates that the boundary layer is not fully recovered to equilibrium within the computational domain. In fact, Martin et al. [30] pointed out that it may take $22-30\delta$ for the boundary layer to recover downstream of the interaction in our case.

Figure 21 plots the isosurface of the discriminant of the velocity gradient tensor, which is a quantity used to identify vortical structures in incompressible flows [31]. The level shown in Fig. 21 is 1×10^{-5} normalized by the maximal value. Figures 22 and 23 are zoomed in views of Fig. 21 upstream and downstream of the ramp corner, respectively. Upstream of the interaction, coherent structures are observed. Near the corner where the interaction takes place, the structures are more chaotic and of smaller extent. There are two possible reasons accounting for the change of the structure extent. First, the structures can be chopped by the strong shock and become smaller. Second, fluids are compressed through the shock, and the vortical structures are also compressed and become smaller. Downstream of the interaction the structures are still small and chaotic. Near the outlet of the computational domain, they start to show a trend of going back to their original size and shape upstream of the corner.

B. Shock Motion and Wall-Pressure Fluctuation

Experiments have shown evidence of large scale, slow shock motion. Ganapathisubramani et al. [19] proposed that very long

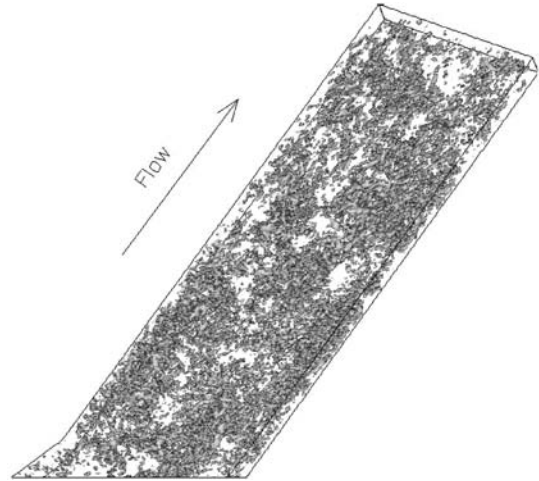


Fig. 23 Isosurface of the discriminant of the velocity gradient tensor downstream of the ramp corner for the DNS. Zoomed visualization of Fig. 21.

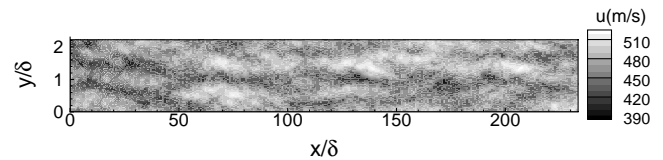


Fig. 24 Rake signal at $z/\delta = 0.2$. The x axis is reconstructed using Taylor's hypothesis and a convection velocity of $0.76U_\infty$. Data are averaged along the streamwise direction in 4δ .

structures of uniform momentum in the incoming boundary layer are responsible for the slow motion. There have been many experimental studies on the turbulent structure of supersonic boundary layers [32–36]. In particular, Ganapathisubramani et al. [37] have shown evidence of the existence of very long structures in supersonic boundary layers. For the signal length that they considered, they observed structures as long as 8δ . In our DNS, we have only 9δ upstream of the corner. However, using the Taylor hypothesis as it is done experimentally [19], the DNS data also exhibit these very long, meandering regions of low momentum. Figure 24 plots contours of normalized mass flux in the logarithmic region ($z = 0.2\delta$) from the DNS. The rake signal is reconstructed using Taylor's hypothesis and a convection velocity of $0.76U_\infty$. Notice that the aspect ratio of x to y is 0.067 in the figure. The presence of these long structures in the DNS data shows that they are an inherent part of a turbulent boundary layer. In addition, we observe evidence of the low frequency shock motion, as shown later.

The shock motion can be inferred from the wall-pressure signal or from monitoring the mass flux in the freestream, for example. Figure 25 plots wall-pressure signals versus time at different

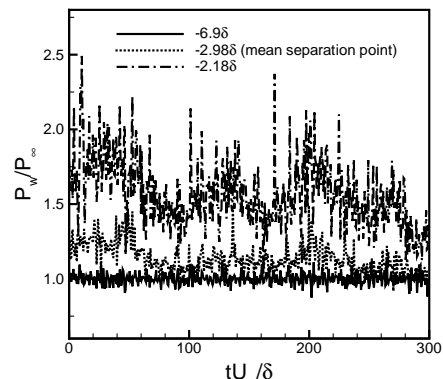


Fig. 25 Wall-pressure signals at different streamwise locations for the DNS.

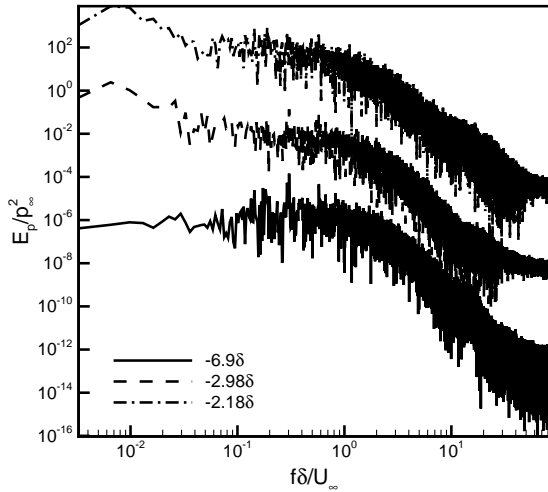


Fig. 26 Spectra of wall-pressure signals at different streamwise locations for the DNS. The spectra for the signals at $x = -2.98\delta$ and $x = -2.18\delta$ are multiplied by 10^3 and 10^6 , respectively.

streamwise locations. The length of the signals is about $300\delta/U_\infty$. For the signal at $x = -2.18\delta$, the wall pressure shows a range of frequencies, including a low frequency mode. The magnitude of the signal varies from about 1.2 to 2.0 in a periodic manner, indicating that the shock is moving upstream and downstream around that point. It should be pointed out that the intermittent character of the wall-pressure signals from the DNS is not as strong as that observed in higher Reynolds number experiments. This may be due to the Reynolds number difference. When the Reynolds number is low, which is the case for the current DNS, viscous effects are more prominent, and the shock does not penetrate into the boundary layer as deeply as for higher Reynolds number cases. In fact, it is observed from the DNS data that the shock is diffused into a compression fan-type structure near the shock foot region. Figure 26 plots the energy spectra for the same wall-pressure signals. To avoid overlapping, the spectra for the signals at $x = -2.98\delta$ and $x = -2.18\delta$ are multiplied by 10^3 and 10^6 , respectively. In the incoming boundary ($x = -6.9\delta$), the most energetic frequency is around $0.1-1U_\infty/\delta$. However, for the other two signals, the most energetic frequency is much lower. At $x = -2.98\delta$, the spectrum has a peak at frequency equal to $0.007U_\infty/\delta$, which corresponds to a time scale of $140\delta/U_\infty$. For the signal at $x = -2.18$, the most energetic frequency ranges from $0.007U_\infty/\delta$ to $0.01U_\infty/\delta$, corresponding to a time scale of $100-140\delta/U_\infty$. The dimensionless frequency computed from Eq. (1) is between 0.03 to 0.043 for the last two signals, which is consistent with what Dussauge et al. [17] found based on experimental data. Recall that the recycling station is located at 4.5δ downstream of the inlet in the DNS. It is doubted that this can impose

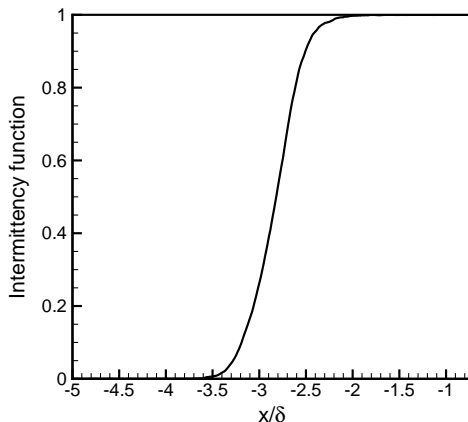


Fig. 27 Intermittency function computed from wall pressure for the DNS.

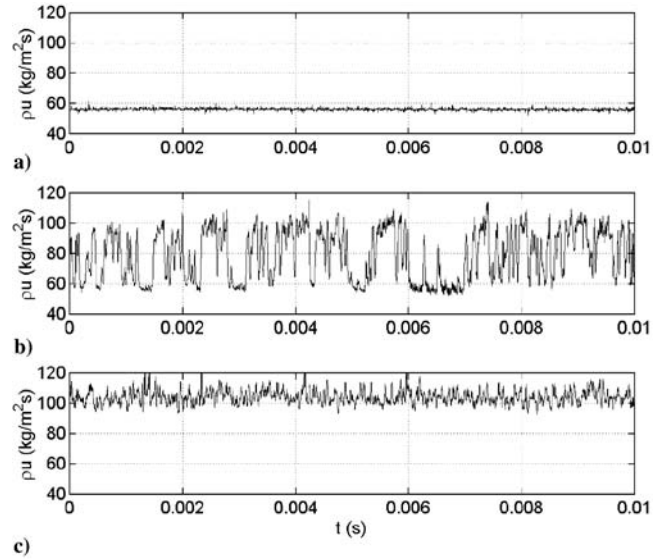


Fig. 28 Mass-flux signals at different streamwise locations from Weiss and Chokani [38]: a) sensor positioned upstream of the shock; b) sensor positioned at the mean shock location; c) sensor positioned downstream of the shock.

a forcing frequency of about $0.2U_\infty/\delta$ on the flow. Figure 26 shows that none of the signals has a dominant frequency near this specific value. Figure 27 plots the intermittency function computed from wall pressure. It is defined as the fraction of time that the wall pressure at a location is greater than a threshold. Here the threshold value used is $1.2P_\infty$. The inverse maximum slope of the intermittency function is 1.7δ . The intermittency profile shifts in the streamwise direction with different threshold value. However, its shape is not affected much by the threshold.

The motion of the shock can also be measured in the freestream. For example, Weiss and Chokani [38] used mass-flux signals along the streamwise direction at a location of 1.5δ away from the wall. Figure 28 plots three mass-flux signals measured in the experiments of Weiss and Chokani [38]. The signal measured at the mean shock location shows an intermittent character. We use the same method by Weiss and Chokani. The mass-flux signals are measured at different streamwise locations with a distance of 2δ away from the wall. Figure 29 plots three mass-flux signals normalized by the freestream quantities. The characteristics of the signals are similar to those observed in Fig. 28. The solid line is a signal measured at a location upstream of the shock. The magnitude of mass flux is about 1.1 for this signal. The dash-dotted line is a signal measured downstream of the shock. The mass flux fluctuates around 1.8. The dotted line data are measured inside the shock motion region. The magnitude of the signal varies between that of the solid line and dash-dotted line, indicating that the shock moves upstream and downstream of this point. Notice that in Fig. 28 the length of the signals is about

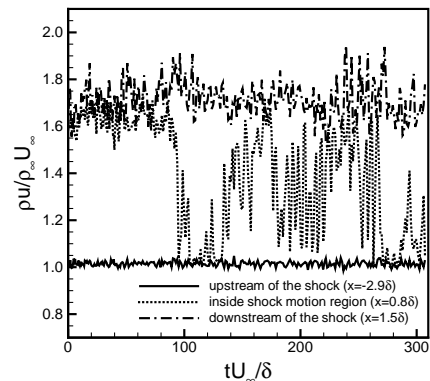


Fig. 29 Mass-flux signals at different streamwise locations at $z = 2\delta$ for the DNS.

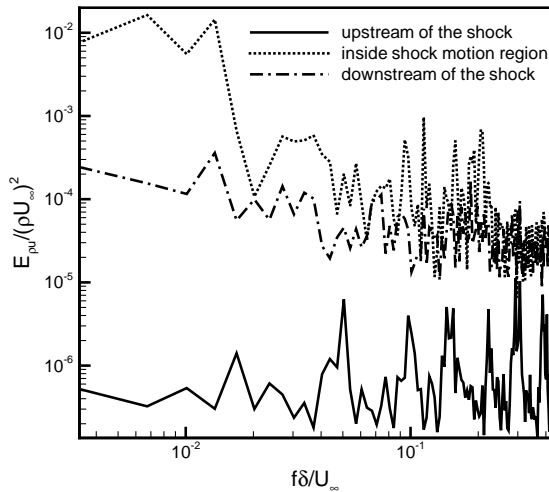


Fig. 30 Spectra of mass-flux signals at different streamwise locations for the DNS.

$1200\delta/U_\infty$, which is nearly 4 times longer than that from the DNS. Also the Mach number in the experiments is 3.5, which is greater than that in the DNS. Figure 30 plots the energy spectra for the three DNS mass-flux signals. The measurement inside the shock motion region is dominated by much lower frequencies relative to those in the other two signals. The spectrum peaks in a frequency range of $0.007\text{--}0.013U_\infty/\delta$, which corresponds to a time scale of $77\text{--}140\delta/U_\infty$. This is consistent with the result obtained from the wall-pressure analysis. Notice that the mass-flux signals have much lower resolution than that of the wall-pressure signals shown in Fig. 25. This is because the wall-pressure signals in Fig. 25 were recorded at each time step during the simulation, while the mass-flux signals were obtained using data that were saved at large time intervals.

The scale of the shock motion can be quantified by the intermittency function proposed by Weiss and Chokani [38]. It is defined as the fraction of time that the shock resides upstream of the measurement location. Thus the intermittency function is 0/1 if a location is always upstream/downstream of the shock. Instantaneous mass flux is used to determine whether a given location is upstream or downstream of the shock. When the instantaneous mass flux is greater than some threshold value, the location is said to be downstream of the shock, and vice versa. The average of the upstream and downstream mass flux is used as the threshold. Figure 31 plots the intermittency function versus streamwise location. For reference, the experimental result from Weiss and Chokani [38] is also plotted. Notice that the experimental data points are shifted in the streamwise direction to make the center of the DNS and experimental intermittency function align with each other. Define the intermittent length of the shock motion as the inverse maximum slope of the intermittency function. Thus, for the DNS, the intermittent length is 0.47δ . For Weiss and Chokani's experiments, the intermittent length is about 0.2δ .

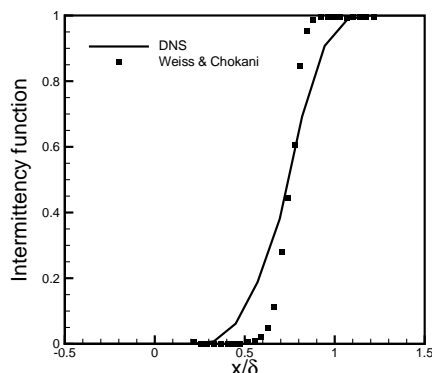


Fig. 31 Intermittency function computed from mass flux for the DNS.

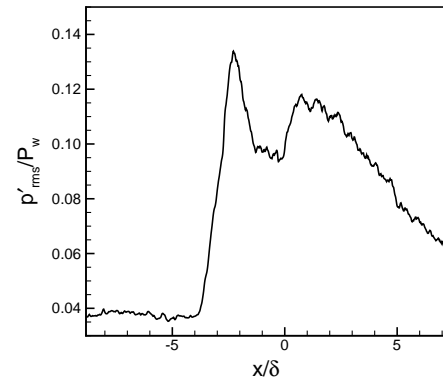


Fig. 32 Normalized wall-pressure fluctuation distribution for the DNS.

It is known that large scale shock motion produces high level wall-pressure fluctuations. Figure 32 plots the normalized wall-pressure fluctuation versus streamwise location. There are two peaks present. The first one is at $x = -2.3\delta$, which is downstream of the mean separation point. It has a magnitude of about 13.5%. The second peak is located at about $x = 0.8\delta$ with a magnitude of about 11.5%. The magnitude of the first peak is lower than that of higher Reynolds number experiments. For example, Dolling and Murphy [4] measured a peak value of about 20%. Currently, no experimental data at the same flow conditions are available for comparison.

VII. Conclusions

A DNS of a 24 deg compression ramp configuration is performed. Applying limiters to the smoothness measurement in the WENO scheme reduces the numerical dissipation. In particular, using a combination of absolute and relative limiters is very effective. The DNS data predict the experiments with a satisfactory accuracy for the upstream boundary layer, mean wall-pressure distribution, size of the separation bubble, velocity profile downstream of the interaction, and mass-flux turbulence intensity amplification.

Numerical schlieren and 3-D isosurfaces of $|\nabla p|$ reveal the structures of the shock system. Turbulence intensities are amplified greatly through the interaction region. In particular, mass-flux turbulence intensity is amplified by a factor of about 5. Reynolds stress components are greatly amplified with amplification factors of about 6–24. As summarized by Smits and Muck [29], there are a few mechanisms that account for turbulence amplification. Across the shock, the turbulence level is increased due to the Rankine–Hugoniot jump conditions and nonlinear coupling of turbulence, vorticity, and entropy waves [39]. The unsteady shock motion also pumps energy from the mean flow into the turbulent fluctuations. In addition, the concave streamline curvature near the ramp corner makes the flow unstable and amplifies the turbulence level [40]. SRA relations are satisfied in the incoming boundary layer. However, in a large neighborhood of the interaction region, the relations are found not valid, especially in the near wall region ($z < 0.5\delta$). This indicates that the boundary layer has not fully recovered to equilibrium downstream of the interaction within the computational domain.

Wall-pressure and mass-flux signals including spectral analysis indicate that there is a low frequency motion of the shock with a characteristic time scale of about $77\text{--}140\delta/U_\infty$, which is consistent with that found in experiments. The magnitude of the shock motion is quantified by the intermittency function computed from mass-flux signals in the freestream. The intermittent length defined as the inverse of the maximum slope of the intermittency function is 0.47δ in the DNS. Dolling and Or [5] found the amplitude of the shock motion of about 0.8δ at higher Reynolds number experiments. The physical mechanism that drives the low frequency motion in the DNS remains to be studied.

Acknowledgments

This work is supported by the U.S. Air Force Office of Scientific Research under grants AF/F49620-02-1-0361 and AF/9550-06-1-

0323. The authors would like to acknowledge A. J. Smits for useful discussions during the assessment of the accuracy of the numerical data.

References

- [1] Settles, G. S., Vas, I. E., and Bogdonoff, S. M., "Details of a Shock-Separated Turbulent Boundary Layer at a Compression Corner," *AIAA Journal*, Vol. 14, No. 12, 1976, pp. 1709–1715.
- [2] Settles, G. S., Fitzpatrick, T., and Bogdonoff, S. M., "Detailed Study of Attached and Separated Compression Corner Flowfields in High Reynolds Number Supersonic Flow," *AIAA Journal*, Vol. 17, No. 6, 1979, pp. 579–585.
- [3] Settles, G. S., Perkins, J. J., and Bogdonoff, S. M., "Investigation of Three-Dimensional Shock/Boundary-Layer Interactions at Swept Compression Corners," *AIAA Journal*, Vol. 18, No. 7, 1980, pp. 779–785.
- [4] Dolling, D. S., and Murphy, M. T., "Unsteadiness of the Separation Shock Wave Structure in a Supersonic Compression Ramp Flowfield," *AIAA Journal*, Vol. 21, No. 12, 1983, pp. 1628–1634.
- [5] Dolling, D. S., and Or, C. T., "Unsteadiness of the Shock Wave Structure in Attached and Separated Compression Corner Flow Fields," AIAA Paper 83-1715, July 1983.
- [6] Selig, M. S., "Unsteadiness of Shock Wave/Turbulent Boundary Layer Interactions with Dynamic Control," Ph.D. Thesis, Princeton University, Princeton, NJ, 1988.
- [7] Bookey, P. B., Wyckham, C., Smits, A. J., and Martin, M. P., "New Experimental Data of STBLI at DNS/LES Accessible Reynolds Numbers," AIAA Paper 2005-309, Jan. 2005.
- [8] Zheltovodov, A. A., "Advances and Problems in Modeling of Shockwave Turbulent Boundary Layer Interactions," *Proceedings of the International Conference on the Methods of Aerophysical Research*, Institute of Theoretical and Applied Mechanics, Novosibirsk, Russia, 2004, pp. 149–157.
- [9] Knight, D., Yan, H., Panaras, G. A., and Zheltovodov, A., "Advances in CFD Prediction of Shock Wave Turbulent Boundary Layer Interactions," *Progress in Aerospace Sciences*, Vol. 39, Nos. 2–3, 2003, pp. 121–184.
- [10] Adams, N. A., "Direct Numerical Simulation of Turbulent Boundary Layer along a Compression Ramp at $M = 3$ and $Re_\theta = 1685$," *Journal of Fluid Mechanics*, Vol. 420, Oct. 2000, pp. 47–83.
- [11] Rizzetta, D., and Visbal, M., "Large-Eddy Simulation of Supersonic Compression-Ramp Flow by High-Order Method," *AIAA Journal*, Vol. 39, No. 12, 2001, pp. 2283–2292.
- [12] Wu, M., and Martin, M. P., "Direct Numerical Simulation of Shockwave/Turbulent Boundary Layer Interactions," AIAA Paper 2004-2145, June 2004.
- [13] Wu, M., Taylor, E. M., and Martin, M. P., "Assessment of STBLI DNS Data and Comparison against Experiments," AIAA Paper 2005-4895, June 2005.
- [14] Weirs, G. V., "A Numerical Method for the Direct Simulation of Compressible Turbulence," Ph.D. Thesis, University of Minnesota, Minneapolis, MN, 1998.
- [15] Martin, M. P., Taylor, E. M., Wu, M., and Weirs, V., "A Bandwidth-Optimized WENO Scheme for the Effective Direct Numerical Simulation of Compressible Turbulence," *Journal of Computational Physics*, Vol. 220, No. 1, 2006, pp. 270–289.
- [16] Wu, M., and Martin, M. P., "Assessment of Numerical Methods for DNS of Shockwave/Turbulent Boundary Layer Interaction," AIAA Paper 2006-0717, Jan. 2006.
- [17] Dussauge, J. P., Dupont, P., and Devieve, J. F., "Unsteadiness in Shock Wave Boundary Layer Interactions with Separation," *Aerospace Science and Technology*, Vol. 10, No. 2, 2006, pp. 85–91.
- [18] Andreopoulos, J., and Muck, K. C., "Some New Aspects of The Shock-Wave/Boundary-Layer Interaction in Compression-Ramp Flows," *Journal of Fluid Mechanics*, Vol. 180, July 1987, pp. 405–428.
- [19] Ganapathisubramani, B., Clemens, N. T., and Dolling, D. S., "Effects of Upstream Coherent Structures on Low-Frequency Motion of Shock-Induced Turbulent Separation," AIAA Paper 2007-1141, Jan. 2007.
- [20] Martin, M. P., "DNS of Hypersonic Turbulent Boundary Layers. Part 1: Initialization and Comparison with Experiments," *Journal of Fluid Mechanics* (to be published).
- [21] Xu, S., and Martin, M. P., "Assessment of Inflow Boundary Conditions for Compressible Turbulent Boundary Layers," *Physics of Fluids*, Vol. 16, No. 7, 2004, pp. 2623–2639.
- [22] Taylor, E. M., Wu, M., and Martin, M. P., "Optimization of Nonlinear Error Sources for Weighted Essentially Non-Oscillatory Methods in Direct Numerical Simulations of Compressible Turbulence," *Journal of Computational Physics* (to be published).
- [23] Jiang, G., and Shu, C., "Efficient Implementation of Weighted ENO Schemes," *Journal of Computational Physics*, Vol. 126, No. 1, 1996, pp. 202–228.
- [24] Shu, C.-W., and Osher, S., "Efficient Implementation of Essentially Non-Oscillatory Shock-Capturing Schemes, II," *Journal of Computational Physics*, Vol. 83, No. 1, 1989, pp. 32–78.
- [25] Taylor, E., and Martin, M., "Stencil Adaption Properties of a WENO Scheme in Direct Numerical Simulations of Compressible Turbulence," *Journal of Scientific Computing* (to be published).
- [26] Zheltovodov, A. A., Schülein, E., and Horstman, C., "Development of Separation in The Region Where a Shock Interacts with a Turbulent Boundary Layer Perturbed by Rarefaction Waves," *Journal of Applied Mechanics and Technical Physics*, Vol. 34, No. 3, 1993, pp. 346–354.
- [27] Zukoski, E., "Turbulent Boundary Layer Separation in Front of a Forward Facing Step," *AIAA Journal*, Vol. 5, No. 10, 1967, pp. 1746–1753.
- [28] Selig, M. S., Andreopoulos, J., Muck, K. C., Dussauge, J. P., and Smits, A. J., "Turbulent Structure in a Shock Wave/Turbulent Boundary-Layer Interaction," *AIAA Journal*, Vol. 27, No. 7, 1989, pp. 862–869.
- [29] Smits, A. J., and Muck, K. C., "Experimental Study of Three Shock Wave/Turbulent Boundary Layer Interactions," *Journal of Fluid Mechanics*, Vol. 182, Sept. 1987, pp. 291–314.
- [30] Martin, M. P., Smits, A. J., Wu, M., and Ringuette, M., "The Turbulence Structure of Shockwave and Boundary Layer Interaction in a Compression Corner," AIAA Paper 2006-0497, 2006; also *Journal of Computational Physics* (to be published).
- [31] Blackburn, H. M., Mansour, N. N., and Cantwell, B. J., "Topology of Fine-Scale Motions in Turbulent Channel Flow," *Journal of Fluid Mechanics*, Vol. 310, March 1996, pp. 269–292.
- [32] Samimy, M., Arnette, S. A., and Elliott, G. S., "Streamwise Structures in a Turbulent Supersonic Boundary Layer," *Physics of Fluids*, Vol. 6, No. 3, 1994, pp. 1081–1083.
- [33] Smith, M. W., and Smits, A. J., "Visualization of the Structure of Supersonic Turbulent Boundary Layers," *Experiments in Fluids*, Vol. 18, No. 4, 1995, pp. 288–302.
- [34] Spina, E. F., Donovan, J. F., and Smits, A. J., "On the Structure of High-Reynolds-Number Supersonic Turbulent Boundary Layers," *Journal of Fluid Mechanics*, Vol. 222, Jan. 1991, pp. 293–327.
- [35] Cogne, S., Forkey, J., Miles, R. B., and Smits, A. J., "The Evolution of Large-Scale Structures in a Supersonic Turbulent Boundary Layer," *Proceedings of the Symposium on Transitional and Turbulent Compressible Flows*, ASME Fluids Engineering Division, Fairfield, NJ, 1993.
- [36] Dussauge, J. P., and Smits, A. J., "Characteristic Scales for Energetic Eddies in Turbulent Supersonic Boundary Layers," *Proceedings of the Tenth Symposium on Turbulent Shear Flows*, Pennsylvania State University, University Park, PA, 1995.
- [37] Ganapathisubramani, B., Clemens, N. T., and Dolling, D. S., "Large-Scale Motions in a Supersonic Turbulent Boundary Layer," *Journal of Fluid Mechanics*, Vol. 556, June 2006, pp. 271–282.
- [38] Weiss, J., and Chokani, N., "Quiet Tunnel Experiments of Shockwave/Turbulent Boundary Layer Interaction," AIAA Paper 2006-3362, June 2006.
- [39] Anyiwo, J. C., and Bushnell, D. M., "Turbulence Amplification in Shock-Wave Boundary-Layer Interaction," *AIAA Journal*, Vol. 20, No. 7, 1982, pp. 893–899.
- [40] Bradshaw, P., "The Effect of Mean Compression or Dilatation on the Turbulence Structure of Supersonic Boundary Layers," *Journal of Fluid Mechanics*, Vol. 63, April 1974, pp. 449–464.

N. Clemens
Associate Editor